
How Out-of-Equilibrium Phase Transitions can Seed Pattern Formation in Trained Diffusion Models

Luca Ambrogioni
Radboud University,
Donders Institute for Brain, Cognition, and Behaviour

Abstract

Diffusion models generate structure by progressively transforming noise into data, yet the mechanisms underlying this transition remain poorly understood. In this work, we show that pattern formation in trained diffusion models can be explained as an out-of-equilibrium phase transition driven by instabilities in the denoising dynamics. We develop a theoretical framework linking data symmetries and architectural constraints, such as locality and translation equivariance, to the emergence of collective spatial modes. In this view, structure arises when low-frequency modes become unstable, triggering a rapid growth of spatial correlations that organizes noise into coherent patterns. We validate this theory through a combination of analytical models and experiments. In a controlled patch-based model, we observe a sharp increase in correlation length and a simultaneous softening of low-frequency modes at a well-defined critical time, accurately predicted by theory. Similar signatures are found in trained convolutional diffusion models on Fashion-MNIST and in large-scale ImageNet models, where pattern formation coincides with a peak in estimated correlation length and a pronounced weakening of spatial modes. Finally, intervention experiments show that applying guidance precisely at this critical stage significantly improves class alignment compared to applying it at random times, demonstrating that this regime is not only descriptive but functionally important.

1 Introduction

Generative diffusion models have recently emerged as one of the most successful frameworks for high-fidelity image and video synthesis (Sohl-Dickstein et al., 2015; Ho et al., 2020; Song et al., 2021; Karras et al., 2022). Because these models gradually organize structure from disordered noise, they exhibit behavior reminiscent of physical systems. In statistical physics, the abrupt emergence of macroscopic order is often explained by *spontaneous symmetry breaking phase transitions*, also known as critical phase transitions (Landau, 1937; Kadanoff, 1966; Wilson, 1971; Wilson & Fisher, 1972; Stanley, 1971). A canonical example is magnetic ordering in a metal: although the underlying microscopic laws governing the atoms are rotationally symmetric, a magnet below its critical temperature spontaneously ‘selects’ a specific magnetic orientation through the amplification of microscopic fluctuations. This analogy raises a natural question: can symmetry-breaking mechanisms similarly explain pattern formation in generative diffusion models? A key indication comes from (Kamb & Ganguli, 2025), where it was shown that denoising dynamics based solely on locality and translational invariance can already produce complex patterns that closely match those generated by convolutional networks. This observation is particularly compelling, as symmetry and locality are central ingredients in the theory of critical phase transitions. In the last few years, several works show that reverse diffusion does not proceed as a smooth interpolation from noise to data, but rather evolves through distinct dynamical regimes. Several studies interpret the generative process in terms of phase-transition-like behavior, in which the noise-symmetric state becomes unstable and trajectories

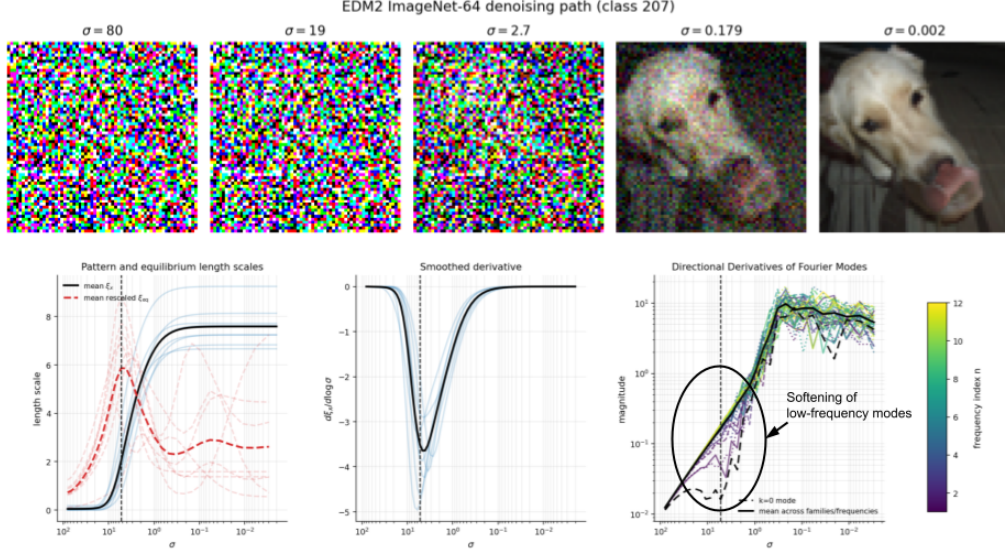


Figure 1: Quantitative analysis of pattern formation dynamics in a trained EDM2 model (Karras et al., 2022, 2024). Top: Example generative denoised trajectory. Left: spatial correlation length $\xi_x(\sigma)$ along several reverse trajectories (transparent blue) and their median (black). The dashed red curves show the equilibrium correlation length estimate $\xi_{\text{eq}}(\sigma)$ obtained from the normalized low-frequency dispersion of the reverse-drift Jacobian. Middle: derivative $d\xi_x/d\log\sigma$ highlighting the rapid growth of spatial coherence near the estimated critical scale. Right: magnitude of median directional derivatives (computed over 8 trajectories) along a range of Fourier modes (colored) together with their median (black) and zero-th mode (dashed) showing the softening of spatial modes. Since EDM2 is variance exploding, all modes become arbitrarily low as σ increases. However, the low frequency modes are strongly suppressed compared to high frequencies at the onset of pattern formation.

concentrate around modes of the data distribution (Biroli et al., 2024; Raya & Ambrogioni, 2024; Sakamoto et al., 2024; Esteban-Casadevall et al., 2026; Sclocchi et al., 2025b; Ambrogioni, 2025; Sclocchi et al., 2025a). Complementary approaches introduce the notion of *critical windows*: short intervals of diffusion time during which specific features of the final sample are determined (Li & Chen, 2024; Li et al., 2025). Despite these advances, a precise connection to the theory of critical phase transitions remains lacking. Existing analyses typically focus either on low-dimensional pitchfork bifurcations (Raya & Ambrogioni, 2024; Biroli et al., 2024) or on highly structured hierarchical models (Sclocchi et al., 2025b,a). Moreover, they are largely restricted to analytically tractable score functions, leaving open the question of how these insights extend to trained neural networks.

The key insight of this work is that the structure of these transitions arises from the interplay between symmetries in the data and architectural constraints of the network, which impose locality, sparsity, and invariance constraints. Building on this perspective, we analyze how pattern formation is triggered by sudden instabilities in low-frequency modes of the dynamics—referred to in physics as *soft modes*. This **mode softening** phenomenon is a key prediction of our theoretical framework, as it is a reliable fingerprint of critical transitions in physical systems that can be directly studied in trained neural networks. We show that, in translationally invariant settings, these modes correspond to sinusoidal Fourier components. Their destabilization leads to the rapid emergence of structure, which is subsequently amplified by the nonlinear reverse diffusion dynamics. We describe this phenomenon as an out-of-equilibrium phase transition, as it is closely analogous to similar phenomena studied in cosmology and material science (Kibble, 1976).

2 Background on symmetries

We consider data points $x = (x_i)_{i \in \Lambda}$ defined on a discrete spatial lattice Λ (e.g., pixels on an image grid). In the following, we will be particularly interested in the limit of large lattice size $|\Lambda| \rightarrow \infty$, where collective and spatial effects become well-defined. A *symmetry group* G is a set of transformations acting on configurations such that the distribution is invariant: $p_t(gx) = p_t(x)$, $\forall g \in G$. It is useful to distinguish two types of transformations. *Global symmetries* act uniformly on the entire configuration (e.g., $x \mapsto -x$), while *spatial symmetries* act on the lattice structure, such as translations $x_i \mapsto x_{i+a}$. In many machine learning models, especially convolutional architectures, these spatial transformations are built into the model via equivariance. A point x^* is called *symmetric* if it is invariant under all transformations: $gx^* = x^*$, $\forall g \in G$. Such points correspond to maximally unstructured configurations. For example, in a dataset with reflection symmetry $x \mapsto -x$, the configuration $x = 0$ is symmetric, while nonzero patterns are mapped into each other. In diffusion models under symmetries, symmetric points act as fixed-points of the dynamics and we are concerned with changes in their stability. While what we shall discuss can be applied to any symmetry group, in all our analysis we will consider the simple symmetry Z_2 : $x \mapsto -x$, which flips the value of binary pixels.

3 Background on bifurcations in generative diffusion models

Diffusion models generate samples by learning to reverse a gradual corruption of the data distribution with Gaussian noise. Let $p_{\text{data}}(x_0)$ denote the data distribution. In the variance-preserving (VP) formulation (Song et al., 2021), the forward process follows $dx_t = -\frac{1}{2}\beta(t)x_t dt + \sqrt{\beta(t)}dW_t$, whose solution can be written $x_t = \alpha(t)x_0 + \sigma(t)\epsilon$, $\epsilon \sim \mathcal{N}(0, I)$, with $\alpha(t) = \exp\left(-\frac{1}{2}\int_0^t \beta(s) ds\right)$, $\sigma^2(t) = 1 - \alpha(t)^2$. Given data $\{x_j\}_{j=1}^N$, a score network $s_\theta(x, t)$ is trained with denoising score matching (Ho et al., 2020). The nonparametric optimum corresponds to the empirical score

$$\nabla \log \hat{p}_t(x_t) = \sum_{j=1}^N w_j(x_t) \nabla_{x_t} \log p_t(x_t^j | x_0^j), \quad (1)$$

where $w_j(x_t) = p(x_0 = x_0^j | x_t) \propto p_t(x_t | x_0^j)$ are normalized Bayesian weights. Once the score is learned, samples are generated by the reverse-time SDE

$$dx_t = \left[-\frac{1}{2}\beta(t)x_t - \beta(t)s_\theta(x_t, t) \right] dt + \sqrt{\beta(t)}d\bar{W}_t. \quad (2)$$

We denote the reverse drift in the VP setting by $b(x, t) := -\frac{1}{2}\beta(t)x - \beta(t)s_\theta(x, t)$, so that the Jacobian of the reverse drift is $J(x, t) := \partial b(x, t)/\partial x$. From a physics perspective, this is an annealed process since t has both the role of dynamic time and effective temperature of the potential. As we shall see, this is what causes out-of-equilibrium phase transitions in the generative dynamics. We will now formalize the theory of symmetry breaking outlined in (Raya & Ambrogioni, 2024) and (Biroli et al., 2024; Achilli et al., 2026; Handke et al., 2026). For simplicity, consider a symmetric dataset consisting of two prototypes, $p_{\text{data}}(x) = \frac{1}{2}\delta(x - \mu) + \frac{1}{2}\delta(x + \mu)$, with $\mu \in \mathbb{R}^N$. After Gaussian noising with variance $\sigma^2(t)$, the forward marginal becomes a two-component Gaussian mixture whose log-density can be written as

$$\log \hat{p}_t(x) = -\frac{1}{2\sigma^2(t)}\|x\|^2 + \log \cosh\left(\frac{\langle \mu, x \rangle}{\sigma^2(t)}\right) + \text{const}. \quad (3)$$

The nonlinearity depends only on the global projection $\langle \mu, x \rangle$, so the empirical geometry couples all coordinates through a single collective mode. Linearizing the score at the symmetric fixed point $x = 0$ yields the reverse drift Jacobian

$$J(0, t) = -\left(\frac{1}{2} + \frac{1}{\sigma^2(t)}\right)I + \frac{1}{\sigma^4(t)}\mu\mu^\top. \quad (4)$$

Its spectrum consists of an $(N - 1)$ -fold degenerate stable eigenvalue and a single eigenvalue along the direction of μ . The first instability occurs when this eigenvalue crosses zero, so the unstable

manifold is one-dimensional. Projecting the deterministic drift component of the reverse dynamics onto this direction and defining $m = \frac{\langle \mu, x \rangle}{\|\mu\|^2}$, one obtains, to leading order, the reverse differential equation

$$\dot{m} = -g(t)^2 r(t) m - u m^3, \quad r(t) = \frac{\sigma^2(t) + 2}{2\sigma^2(t)} - \frac{\|\mu\|^2}{\sigma^4(t)}. \quad (5)$$

When $r(t)$ changes sign, a supercritical pitchfork bifurcation occurs with equilibria $m_{\pm} \sim \sqrt{-r(t)}$.

We now consider a dataset of M centered prototypes $\{\mu_m\}_{m=1}^M$, with $\sum_m \mu_m = 0$. The point $x = 0$ remains a symmetric fixed point, and the Jacobian of the reverse drift takes the form

$$J(0, t) = -\left(\frac{1}{2} + \frac{1}{\sigma^2(t)}\right) I + \frac{1}{\sigma^4(t)} \sum_{m=1}^M \mu_m \mu_m^\top. \quad (6)$$

Hence the stability is governed by the empirical second-moment matrix $C = \sum_{m=1}^M \mu_m \mu_m^\top$. Since $J(0, t)$ is an affine function of C , both share the same eigenvectors, and instabilities occur when $\lambda_k(t) = a(t) + c(t)\lambda_k(C)$ cross zero. The unstable directions are therefore given by the leading eigenspaces of C . If the prototypes are approximately orthogonal, i.e. $\langle \mu_m, \mu_n \rangle \approx 0$ for $m \neq n$, then each μ_m is an approximate eigenvector of C , so the unstable directions are approximately aligned with individual patterns.

4 From memorization to pattern formation through architectural constraints

The goal of this section is to understand how architectural structure constrains the symmetry-breaking mechanisms that can appear in the learned dynamics. We begin by briefly recalling the learning setup. Let $\mathcal{F} = \{s_\theta(\cdot, t) \mid \theta \in \Theta\}$ denote the class of score fields realizable by a given neural architecture. The parameters are learned by minimizing the denoising score-matching objective

$$\mathcal{L}(\theta) = \mathbb{E}_{t, x_0, \epsilon} \left[\|s_\theta(x_t, t) - \nabla_{x_t} \log p_t(x_t \mid x_0)\|^2 \right], \quad (7)$$

where $x_t = \alpha(t)x_0 + \sigma(t)\epsilon$ is the forward diffusion process. In general, we can conceptualize the result of training as a non-linear projection of the empirical vector field onto the set of vector fields allowed by the model class: $\mathcal{P}[\nabla_{x_t} \log p_t(\cdot \mid x_0)] = s_{\theta^*}(\cdot, t)$ where θ^* depends implicitly on the global empirical score. The training dynamics of deep nets, as captured by the mapping \mathcal{P} , is extremely complex. However, the instability structure is fundamentally constrained by the architecture class, which can be used to infer several generic properties of this mapping.

If the function class \mathcal{F} were sufficiently expressive, minimizing this loss would allow the network to recover the empirical score field associated with the dataset. However, in architectures with bounded receptive fields, each coordinate interacts only with a fixed-size neighborhood Ω . The resulting Jacobian therefore contains nonzero entries only within a band determined by the receptive field. The number of independent couplings per site is $O(|\Omega|)$, where $|\Omega|$ is the number of sites in the receptive field. Consequently, the total number of free parameters in the linearized operator scales as $O(N|\Omega|)$, rather than $O(N^2)$. Isolating a specific dense vector $v \in \mathbb{R}^N$, as an eigenvector of a matrix generically requires imposing $O(N)$ independent constraints on the operator entries. An even stronger restriction arises when the architecture is translation equivariant, as in convolutional score networks. In that case, in the large image limit, the Jacobian becomes a convolution operator. Such operators are diagonalized by spatial Fourier modes. Therefore

$$J(0, t) = \sum_k \lambda(k, t) e^{ik} e^{-ik^\top}. \quad (8)$$

where the sum ranges all vectors of spatial frequencies k allowed by the grid, forming a discrete Fourier basis over spatial modes. As standard in Fourier analysis, the complex exponential here is a convenient way to organize spatial sine and cosine waves. Note that e^{ik} is a vector since k is a vector.

From this diagonalization results, it follows that the instability structure of translationally invariant architectures (in the large image limit) is necessarily aligned with spatial frequency components, instead than with the individual data-points like in the empirical case. In these soft mode instabilities, the Jacobian values corresponding to a whole group of low-frequency components vanish at the same

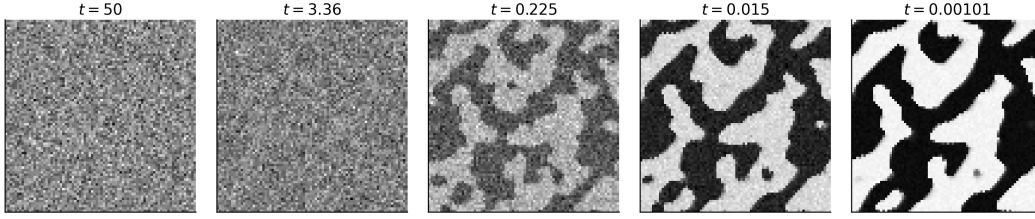


Figure 2: Five snapshots of the evolving configuration are shown at logarithmically spaced times along the reverse diffusion path.

time. Writing the configuration as $x(r, t) = \sum_k q_k(t) e^{ik \cdot r}$, the linearized dynamics decouples mode by mode,

$$\dot{q}_k(t) = \lambda(k, t) q_k(t), \quad (9)$$

where $\lambda(k, t)$ are the eigenvalues of the reverse-drift Jacobian. The onset of pattern formation is thus controlled by the structure of this spectrum. As we shall see in the next section, for local translationally invariant architectures, the spectrum is smooth at small k and admits the expansion $\lambda(k, t) = -r(t) - \kappa(t)k^2 + O(k^4)$, which defines an *effective mass* $r(t)$ and *stiffness* $\kappa(t) > 0$. This jargon is borrowed from physics, where r plays the role of the mass of particles or particle-like perturbations (e.g. sound waves) since it determines the amount of energy needed to put them in motion. In this representation, unstable modes (soft modes) are precisely those for which $\lambda(k, t)$ approaches zero. The critical time t_c is therefore defined by the condition $\lambda(0, t_c) = 0$, or equivalently $r(t_c) = 0$. The dynamics across this point is governed by a sign change of the mass term. For $r(t) > 0$, all eigenvalues are negative and fluctuations decay. For $r(t) < 0$, the modes acquire positive growth rates and grow exponentially. The instability is therefore not confined to a single mode but involves a finite band of low-frequency modes whose width increases with $|r(t)|$. This band instability provides a direct mechanism for pattern formation.

5 Analysis of the patch score model

We now analyze a tractable analytic example illustrating how architectural locality converts global symmetry-breaking instabilities into spatially extended critical phenomena. We consider the minimal \mathbb{Z}_2 -symmetric dataset $x_0 = \pm 1$ with equal probability. The empirical score is

$$\nabla \log \hat{p}_t(x) = -\frac{x}{\sigma^2(t)} + \frac{\alpha(t)}{\sigma^2(t)} \mathbb{E}[x_0 | x], \quad (10)$$

which is intrinsically nonlocal. Following Kamb & Ganguli (2025), we impose a locality constraint by restricting the score to

$$s_i(x, t) = f_t(x_{\Omega_i}), \quad x_{\Omega_i} = \{x_{i+u} : u \in \Omega\}. \quad (11)$$

where f_t is an arbitrary function. The score-matching solution can then be computed analytically:

$$s_i(x, t) = \frac{1}{\sigma^2(t)} \left[\alpha(t) \tanh\left(\frac{\alpha(t)}{\sigma^2(t)} S_i(x)\right) - x_i \right], \quad (12)$$

with $S_i(x) = \sum_{u \in \Omega} x_{i+u}$. We can now study the dynamics of this very simple 'learned' score model by analyzing the instability around the symmetric state $x^* = 0$.

A Taylor expansion around the symmetric state yields

$$s_i(x, t) = -\frac{x_i}{\sigma^2(t)} + \frac{\alpha^2(t)}{\sigma^4(t)} \sum_{u \in \Omega} x_{i+u} - \frac{\alpha^4(t)}{3\sigma^8(t)} \left(\sum_{u \in \Omega} x_{i+u} \right)^3 + \dots \quad (13)$$

To relate this expression to the soft-mode picture of Sec. 5, it is essential to consider the large-system limit. Around the symmetric point, the Jacobian of the reversed drift is given by the convolution operator

$$J_{ij}(0, t) = -\left(\frac{1}{2} + \frac{1}{\sigma^2(t)}\right) \delta_{ij} + \frac{\alpha^2(t)}{\sigma^4(t)} \mathbb{I}((j-i) \in \Omega) \quad (14)$$

where \mathbb{I} is equal to one when the condition is respected and zero otherwise. In the thermodynamic limit with translationally invariant patches, $J(0, t)$ is diagonalized by Fourier modes. Writing the patch as a hyper-cubic neighborhood $\Omega = \{u \in \mathbb{Z}^d : |u_\mu| \leq K, \mu = 1, \dots, d\}$, the eigenvectors are plane waves $e^{ik \cdot i}$ and the corresponding eigenvalues are

$$\lambda(k, t) = - \left(\frac{1}{2} + \frac{1}{\sigma^2(t)} \right) + \frac{\alpha^2(t)}{\sigma^4(t)} \sum_{u \in \Omega} e^{ik \cdot u}. \quad (15)$$

The first term is the spatially uniform spherical contribution coming from the Gaussian component of the score, while the second term is the local convolution kernel induced by the architectural constraint. For the hypercubic patch, the Fourier symbol factorizes and the full analytic spectrum is

$$\lambda(k, t) = - \left(\frac{1}{2} + \frac{1}{\sigma^2(t)} \right) + \frac{\alpha^2(t)}{\sigma^4(t)} \prod_{\mu=1}^d \frac{\sin((K + \frac{1}{2})k_\mu)}{\sin(k_\mu/2)} \quad (16)$$

with q in the Brillouin zone. In particular, the most unstable mode is the uniform mode $q = 0$, with the $\lambda(0, t)$ eigenvalue being given by $-\lambda(0, t) = r(t) = \left(\frac{1}{2} + \frac{1}{\sigma^2(t)} \right) - \frac{\alpha^2(t)}{\sigma^4(t)} (2K + 1)^d$. At the mean-field level, where we do not consider the effect of stochastic fluctuations around the symmetric point, this gives us the following expression for the critical noise level:

$$\lambda(0, t_c) = 0 \implies \left(\frac{1}{2} + \frac{1}{\sigma^2(t_c)} \right) = \frac{\alpha^2(t_c)}{\sigma^4(t_c)} (2K + 1)^d \quad (17)$$

To investigate soft non-zero frequency modes, we expand (16) for small wave-vector, which gives the low-frequency dispersion of the Jacobian is

$$\lambda(k, t) = -r(t) - \kappa(t)|k|^2 + O(|k|^4). \quad (18)$$

This shows that locality converts the mean-field bifurcation into a dispersive instability with a finite stiffness $\kappa(t) = \frac{\alpha^2(t)}{\sigma^4(t)} \frac{K(K+1)}{6} (2K + 1)^d$. The instability therefore remains maximal at $q = 0$, but extends over a continuum of nearby long-wavelength modes in the large-system limit, producing the spatially extended critical regime characteristic of local score architectures.

5.1 Coarse graining, continuum dynamics and renormalization

To fully relate this expression to the soft-mode picture of Sec. 5, it is useful to consider the large-system (continuum) limit. On a finite lattice, instabilities correspond to isolated eigenvalues of the linearized operator crossing zero. In contrast, in the large image limit, translation equivariance implies a dispersion relation $\lambda(k, t)$ that is smooth in k . So instability occurs through the simultaneous softening of a band of low-frequency modes. This structure underlies the emergence of a growing correlation length and cannot be fully captured at the purely discrete level. For configurations varying slowly on the scale of Ω , we expand $\sum_{u \in \Omega} x_{i+u} \approx |\Omega| x_i + \kappa(t) \nabla^2 x_i$, which gives the reverse drift $s(x, t) + \frac{1}{2}x \approx -r(t)x + \kappa(t) \nabla^2 x - u(t)x^3$, with $u(t) = \frac{\alpha^4(t)}{3\sigma^8(t)} (2K + 1)^{3d}$. In the continuous limit, the deterministic reverse dynamics $\partial_t x = -\frac{1}{2}x - s(x, t)$ then takes the form

$$\partial_t x = a(t)x + \kappa(t) \nabla^2 x - u(t)x^3, \quad (19)$$

This is a stochastic evolution equation that describes the dynamics of the system at low-frequencies, where we can neglect the effect of the original grid (e.g. the discrete pixels in an image). The derivation above yields a deterministic dynamics in which the onset of the instability is controlled by the coefficient $r(t)$. In the stochastic reverse process, however, fluctuations modify this prediction. This is a very profound topic that touches on the theory of renormalization and we are only going to consider it briefly at a superficial level. To make the effect of fluctuations explicit, we decompose the field into a smooth component and fluctuations, $x = \bar{x} + \delta x$, and expand the cubic term: $x^3 = \bar{x}^3 + 3\bar{x}^2 \delta x + 3\bar{x}(\delta x)^2 + (\delta x)^3$. Averaging over fluctuations at fixed \bar{x} and using symmetry ($\langle \delta x \rangle = 0$) gives $\langle x^3 \rangle \approx \bar{x}^3 + 3\bar{x} \langle \delta x^2 \rangle$. Substituting into the coarse-grained dynamics yields

$$\partial_t \bar{x} = a(t)\bar{x} + \kappa(t) \nabla^2 \bar{x} - u(t)\bar{x}^3 - 3u(t) \langle \delta x^2 \rangle \bar{x}. \quad (20)$$

Thus fluctuations re-normalize the linear coefficient, defining an effective mass term

$$r_{\text{eff}}(t) = r(t) + 3u(t) \langle \delta x^2 \rangle. \quad (21)$$

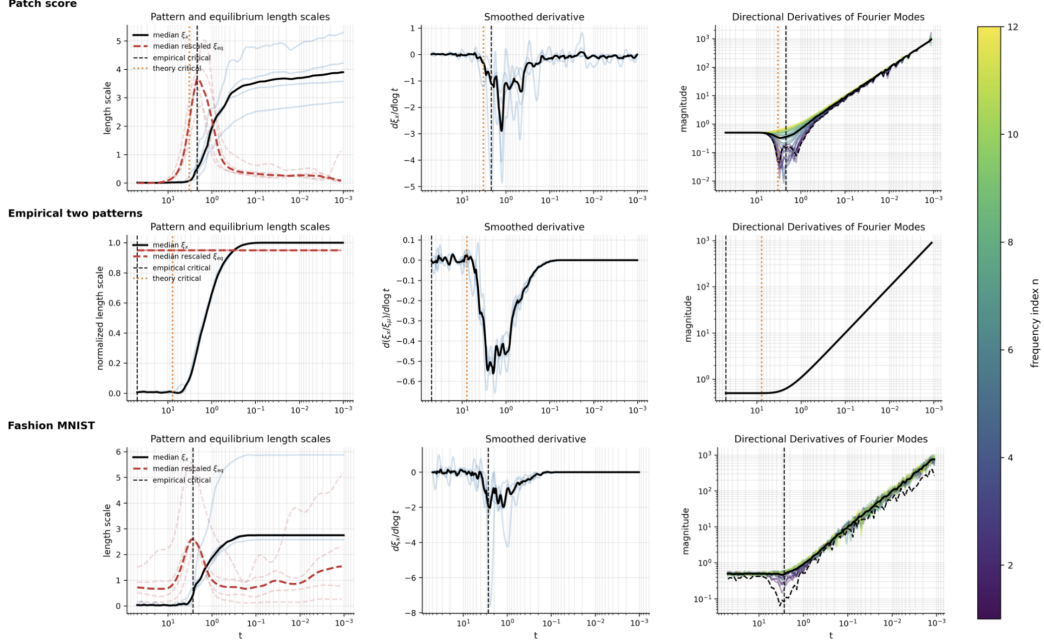


Figure 3: Quantitative analysis of pattern formation dynamics in patch score model (top), two patterns empirical score (middle), trained Fashion MNIST ConvNet (bottom) Left: spatial correlation length $\xi_x(t)$ along several reverse trajectories (transparent blue) and their median (black). The dashed red curves show the equilibrium correlation length estimate $\xi_{\text{eq}}(t)$ obtained from the normalized low-frequency dispersion of the reverse-drift Jacobian. Middle: derivative $d\xi_x/d \log t$ highlighting the rapid growth of spatial coherence near the critical time. Right: magnitude of median directional derivatives (computed over 8 trajectories) along a range of Fourier modes (colored) together with their mean (black) and the zero-th frequency mode (dashed), showing the softening of spatial modes near the transition.

The variance $\langle \delta x^2 \rangle$ can be approximately estimated from the linearized dynamics. This leads to a growth of $\langle \delta x^2 \rangle$ near the instability, and therefore to a significant shift in the effective mass. Since $\langle \delta x^2 \rangle > 0$, the instability condition is shifted from $r(t) = 0$ to $r_{\text{eff}}(t) = 0$, implying that the effective transition occurs earlier than the mean-field prediction.

6 Experiments on patch score model

We consider a two-dimensional patch model on a periodic 80×80 lattice. The generative model consists of 5×5 binary patches drawn from a discrete dictionary. The dictionary contains eight random patterns sampled from $\{\pm 1\}^{5 \times 5}$ together with their sign-flipped copies to enforce a global \mathbb{Z}_2 symmetry. In addition, two global patterns consisting of all +1 and all -1 patches are included. The prior probability mass is concentrated on the global patterns ($p = 0.9$ total), while the eight random patterns share the remaining mass ($p = 0.1$ total). We simulate the reverse dynamics of the variance-preserving diffusion process with constant noise rate $\beta = 1$. The reverse SDE is integrated numerically on a logarithmic time grid from $T = 50$ to $t = 10^{-3}$ using 2000 integration steps. The score function $s(x, t)$ is computed analytically from the full patch posterior without linearization. Figure 2 shows the patch dictionary together with a representative reverse denoising trajectory. At early times ($t \approx T$) the system is dominated by Gaussian noise. As time decreases, local patch evidence accumulates and coherent spatial domains begin to form. Eventually the system locks into large-scale binary regions corresponding to the dominant global patterns.

To quantify the emergence of spatial structure we measure the correlation length of the binarized field $\tilde{x} = \text{sign}(x)$ along the reverse trajectory. The spatial correlation length $\xi_x(t)$ is estimated from the radially averaged autocorrelation function of \tilde{x} . To obtain stable estimates of the temporal derivative we first smooth $\xi_x(t)$ with a Gaussian kernel before computing $d\xi_x/d \log t$. Figure 3 (left) shows

$\xi_x(t)$ for several independent reverse trajectories (transparent curves) together with their median (black curve). The correlation length remains close to zero at large noise levels and increases rapidly once spatial structure begins to form. The middle panel shows the derivative $d\xi_x/d\log t$, which exhibits a pronounced peak near the onset of pattern formation. The vertical dashed line indicates the critical time $t_c \approx \log(26)$, which corresponds to the point where spatial modes of the reverse dynamics begin to soften.

Linearized dynamics and equilibrium correlation length. To understand the origin of this transition we analyze the linearized reverse drift along the denoising trajectory. Directional derivatives of the drift are computed along Fourier modes $v_k(x, y) = \cos(kx), \cos(ky), \cos(k(x+y))$. These directional derivatives provide estimates of the eigenvalues of the Jacobian of the reverse drift. The right panel of Fig. 3 shows the magnitude of these directional derivatives for several spatial modes. As the reverse process approaches the critical region the low-frequency modes soften simultaneously, producing a pronounced minimum near t_c . This softening signals the emergence of long-range spatial fluctuations. Using these measurements we estimate an approximate equilibrium correlation length $\xi_{\text{eq}}(t)$ associated with fluctuations around the instantaneous denoising branch. To obtain a stable estimate we consider the normalized low-frequency dispersion of the Jacobian,

$$\frac{\lambda_n(t)}{\lambda_0(t)} \approx 1 + \xi_{\text{eq}}(t)^2 (nk_{\min})^2, \quad (22)$$

where $\lambda_n(t)$ denotes the directional derivative along the n -th Fourier shell and $k_{\min} = 2\pi/L$. This normalization removes the rapidly increasing overall stiffness of the dynamics at small t and isolates the spatial curvature of the spectrum. Fitting this relation across the lowest Fourier shells provides an estimate of $\xi_{\text{eq}}(t)$. Note that this quantity is not a direct observable correlation due to the out-of-equilibrium nature of the dynamics, it is instead a proxy to quantify the softening of the modes at criticality. The resulting curves are shown as dashed red lines in Fig. 3 (top). Individual trajectory estimates are shown in transparency while the median estimate is plotted in dashed red. The inferred equilibrium correlation length grows prior to the critical point, peaks close to the minimum of the soft modes, and subsequently decreases again as the dynamics locks into a stable pattern. This behavior explains why the observed pattern correlation length begins increasing before the critical time: the underlying spatial modes start softening earlier, amplifying long-wavelength fluctuations before the system fully transitions into a patterned state. On the other hand, in Fig. 3 (middle) we see the same quantities plotted for an empirical score with two patterns $-\mu$ and μ with $\mu(x, y) = \text{sign}(\cos(\frac{2\pi}{48}(x+2y)))$. In this case, the inferred correlation length is roughly constant and there is not visible softening of low frequency modes, with the critical times corresponding to a one-dimensional bifurcation.

7 Experiments on real equivariant architectures

In supplementary section B, we show that critical transitions are present in arbitrary translationally equivariant and local architectures as far as the data respects some symmetries. Even when the symmetries are not exact, like in real images, the phenomenon of critical mode softening can be confirmed qualitatively on trained ConvNets. We trained a model on the dataset FashionMNIST (Xiao et al., 2017), the details are given in Supp.D. We binarized the data so as to preserve the same approximate Ising-like symmetry group. Figure 3 (bottom) shows that the results are strikingly similar to the theoretical model, with a clear peak of equilibrium correlation length at the estimated critical point, a general softening of low frequency modes in a critical region and a sudden onset of pattern formation starting at the estimated critical point. This qualitative agreement is significant. The patch model and the trained U-Net differ radically in their microscopic description: one is a simplified analytic system with explicit patch interactions, while the other is a high-dimensional non-linear neural network trained on real data with partial symmetries. Yet both systems exhibit the same dynamical signatures predicted by the theory, mode softening, abrupt spatial structure formation, and rapidly growing correlations. Supp. Fig 7 shows that this qualitative behavior is approximately preserved even when the model is trained on non-binarized data (under the same specifications), showing that the phenomenology is robust to changes in the symmetry structure of the data. More strikingly, as shown in Fig.1 given at the beginning of the paper, a similar phenomenology can be observed in very complex EDM2 models. In this EDM setting, the reverse dynamics is parameterized by the noise scale σ rather than the VP time variable t , with $\sigma = \sigma(t)$ under the corresponding noise

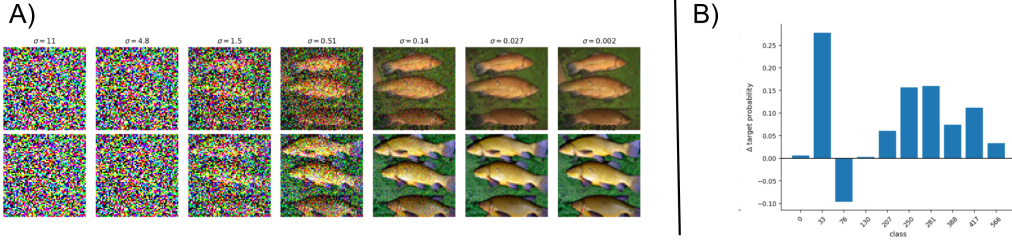


Figure 4: Results of pulse guidance experiment. A) Example image generated by the EDM2 model without critical guidance pulse (top) and with critical guidance pulse (bottom). B) Difference in class alignments (DINOv2 score) between critical pulse guidance and random pulse guidance for difference classes. Critical pulses show higher alignment for almost all tested classes.

schedule. In this case, we again see a clear softening of the low frequency modes in a critical region. The inferred correlation length has a clear peak and corresponds with the onset of pattern formation. Note that the initial slope of the median mode response is due to the fact that EDM2 uses a variance exploding model, meaning that the system does not equilibrate and instead it spreads out, leading to a linear softening of all modes at large noise scale. The EDM2 experiment is described in detail in supp.E.

Guidance pulse experiments. To test whether the critical regime identified by our dynamical analysis is functionally relevant for generation, we performed a pulse-guidance intervention on a pretrained EDM2 ImageNet diffusion model. The key idea is to apply classifier-free guidance (Ho & Salimans, 2022) only within a short window of noise scales during the reverse trajectory, rather than throughout the entire sampling process. For each class, we first estimated the reverse-diffusion dynamics and extracted the equilibrium correlation length proxy $\xi_{\text{eq}}(\sigma)$ from the normalized low-frequency dispersion of the Jacobian of the reverse drift. To reduce noise, the critical scale was not estimated separately for each class; instead, we aggregated the unguided trajectories across all classes and defined a single estimated global "critical" scale $\sigma_c = \arg \max_{\sigma} \xi_{\text{eq}}(\sigma)$. This provides an empirical estimate of the window in which long-wavelength modes are maximally softened. We then compared two intervention strategies. In the *critical-pulse* condition, a strong pulse of classifier-free guidance was applied only within a narrow interval centered at σ_c . In the *random-pulse* condition, an equally strong pulse with the same duration was applied at a random noise scale, sampled uniformly in σ . For each of 10 ImageNet classes we generated 40 samples per condition. Final samples were scored using a pretrained DINOv2 ImageNet classifier (Oquab et al., 2023), and class alignment was quantified by the target-class logit and probability. Details are given in Supp. F. Figure 4 shows that, across classes, pulses delivered near the critical window systematically improved class alignment relative to pulses delivered at random times. This shows that the regime identified by the low-frequency softening analysis is not merely descriptive: it marks a stage of the reverse dynamics where perturbations have higher leverage over the emerging large-scale structure.

8 Conclusion and Limitations

Our theory and results suggest that concepts from non-equilibrium statistical physics, instabilities, soft modes, and effective field theories provide a useful organizing framework for understanding trained diffusion models under architectural constraints such as translational equivariance. Overall, in diffusion models, the dynamics can always be locally described by a Jacobian and there is a clear unimodal potential in the high-noise limit, making instabilities essentially unavoidable except in trivial cases (Ambrogioni, 2025; Biroli et al., 2024). However, the structure of these instability can differ significantly in models without a strong invariant spacial organization, like in latent diffusion models and stable diffusion. Further work is needed to extent this theoretical framework to more generic architectures and data structures, where the system is not approximately translationally invariant. It is also important to stress that the criticalities described in this paper are our-of-equilibrium instabilities, not equilibrium phase transitions. Since the studied systems is finite and the generative system does not fully thermalize, they give raise to finite cross-overs without a full divergence of thermodynamic potentials. This is formally very similar to Kibble-Zurek theory, where, like in generative diffusion, the control parameter (e.g. temperature) is linearly linked to the dynamic time (Kibble, 1976).

9 Acknowledgments

The author wishes to thank the participants of the Aspen Winter Conference Theoretical Physics for Artificial Intelligence (2026) for the insightful discussions that contributed to the ideas developed in this work. In particular, the author is grateful to Mason Kamb and Akhil Premkumar.

The author also acknowledges the role of GPT-5.4 in conceptual brainstorming, experimental implementation, and collaborative drafting of this manuscript. The system served as a high-fidelity intellectual partner, assisting in refining and evaluating the underlying physical theory, as well as in implementing the experimental code. However, the final synthesis, theoretical framing, and verification of all claims remain the sole responsibility of the author.

References

- Beatrice Achilli, Marco Benedetti, Giulio Biroli, and Marc Mézard. Theory of speciation transitions in diffusion models with general class structure. *arXiv preprint arXiv:2602.04404*, 2026. doi: 10.48550/arXiv.2602.04404.
- Luca Ambrogioni. The statistical thermodynamics of generative diffusion models: Phase transitions, symmetry breaking, and critical instability. *Entropy*, 27(3):291, 2025. doi: 10.3390/e27030291.
- Giulio Biroli, Tony Bonnaire, Valentin de Bortoli, and Marc Mézard. Dynamical regimes of diffusion models. *Nature Communications*, 15:9957, 2024. doi: 10.1038/s41467-024-54281-3.
- Maria Esteban-Casadevall, Rafal Karczewski, Alison Pouplin, Søren Hauberg, and Erik J. Bekkers. On the fisher geometry of diffusion models’ latent space. In *ICLR 2026 Workshop on Geometry-grounded Representation Learning and Generative Modeling*, 2026.
- Florian Handke, Dejan Stančević, Felix Koulischer, Thomas Demeester, and Luca Ambrogioni. The entropic signature of class speciation in diffusion models. *arXiv preprint arXiv:2602.09651*, 2026. doi: 10.48550/arXiv.2602.09651.
- Jonathan Ho and Tim Salimans. Classifier-free diffusion guidance. *arXiv preprint arXiv:2207.12598*, 2022. doi: 10.48550/arXiv.2207.12598.
- Jonathan Ho, Ajay Jain, and Pieter Abbeel. Denoising diffusion probabilistic models. In *Advances in Neural Information Processing Systems*, volume 33, pp. 6840–6851, 2020.
- Leo P. Kadanoff. Scaling laws for ising models near tc. *Physics*, 2(6):263–272, 1966. doi: 10.1103/PhysicsPhysiqueFizika.2.263.
- Mason Kamb and Surya Ganguli. An analytic theory of creativity in convolutional diffusion models. In *Proceedings of the 42nd International Conference on Machine Learning*, volume 267 of *Proceedings of Machine Learning Research*, 2025.
- Tero Karras, Miika Aittala, Timo Aila, and Samuli Laine. Elucidating the design space of diffusion-based generative models. In *Advances in Neural Information Processing Systems*, volume 35, pp. 26565–26577, 2022.
- Tero Karras, Miika Aittala, Timo Aila, and Samuli Laine. Analyzing and improving the training dynamics of diffusion models. *arXiv preprint arXiv:2312.02696*, 2024.
- Tom W. B. Kibble. Topology of cosmic domains and strings. *Journal of Physics A: Mathematical and General*, 9(8):1387–1398, 1976. doi: 10.1088/0305-4470/9/8/029.
- Lev D. Landau. On the theory of phase transitions. *Zhurnal Eksperimental’noi i Teoreticheskoi Fiziki*, 7:19–32, 1937.
- Marvin Li and Sitan Chen. Critical windows: Non-asymptotic theory for feature emergence in diffusion models. In *Proceedings of the 41st International Conference on Machine Learning*, volume 235 of *Proceedings of Machine Learning Research*, pp. 27474–27498, 2024.

- Marvin Li, Aayush Karan, and Sitan Chen. Blink of an eye: A simple theory for feature localization in generative models. In *Proceedings of the 42nd International Conference on Machine Learning*, volume 267 of *Proceedings of Machine Learning Research*, pp. 35047–35080, 2025.
- Maxime Oquab, Timothée Darcet, Theo Moutakanni, Huy V. Vo, Marc Szafraniec, Vasil Khalidov, Pierre Fernandez, Daniel Haziza, Francisco Massa, Alaaeldin El-Nouby, Mahmoud Assran, Nicolas Ballas, Wojciech Galuba, Russell Howes, Po-Yao Huang, Shang-Wen Li, Ishan Misra, Michael Rabbat, Vasu Sharma, Gabriel Synnaeve, Hu Xu, Hervé Jégou, and Piotr Bojanowski. Dinov2: Learning robust visual features without supervision. *arXiv preprint arXiv:2304.07193*, 2023.
- Gabriel Raya and Luca Ambrogioni. Spontaneous symmetry breaking in generative diffusion models. *Journal of Statistical Mechanics: Theory and Experiment*, 2024(10):104025, 2024. doi: 10.1088/1742-5468/ad64bd.
- Kotaro Sakamoto, Ryosuke Sakamoto, Masato Tanabe, Masatomo Akagawa, Yusuke Hayashi, Manato Yaguchi, Masahiro Suzuki, and Yutaka Matsuo. The geometry of diffusion models: Tubular neighbourhoods and singularities. In *ICML 2024 Workshop on Geometry-grounded Representation Learning and Generative Modeling*, 2024.
- Antonio Sclocchi, Alessandro Favero, Noam Itzhak Levi, and Matthieu Wyart. Probing the latent hierarchical structure of data via diffusion models. *Journal of Statistical Mechanics: Theory and Experiment*, 2025(8):084005, 2025a. doi: 10.1088/1742-5468/ad64bc.
- Antonio Sclocchi, Alessandro Favero, and Matthieu Wyart. A phase transition in diffusion models reveals the hierarchical nature of data. *Proceedings of the National Academy of Sciences*, 122(1): e2408799121, 2025b. doi: 10.1073/pnas.2408799121.
- Jascha Sohl-Dickstein, Eric Weiss, Niru Maheswaranathan, and Surya Ganguli. Deep unsupervised learning using nonequilibrium thermodynamics. In *Proceedings of the 32nd International Conference on Machine Learning*, pp. 2256–2265, 2015.
- Yang Song, Jascha Sohl-Dickstein, Diederik P. Kingma, Abhishek Kumar, Stefano Ermon, and Ben Poole. Score-based generative modeling through stochastic differential equations. In *International Conference on Learning Representations*, 2021.
- H. Eugene Stanley. *Introduction to Phase Transitions and Critical Phenomena*. Clarendon Press, Oxford, 1971.
- Kenneth G. Wilson. Renormalization group and critical phenomena. i. renormalization group and the kadanoff scaling picture. *Physical Review B*, 4(9):3174–3183, 1971. doi: 10.1103/PhysRevB.4.3174.
- Kenneth G. Wilson and Michael E. Fisher. Critical exponents in 3.99 dimensions. *Physical Review Letters*, 28(4):240–243, 1972. doi: 10.1103/PhysRevLett.28.240.
- Han Xiao, Kashif Rasul, and Roland Vollgraf. Fashion-mnist: a novel image dataset for benchmarking machine learning algorithms. *arXiv preprint arXiv:1708.07747*, 2017. doi: 10.48550/arXiv.1708.07747.

A Explicit Ginzburg–Landau Parameters and mean-field critical time

The parameters of the coarse-grained Ginzburg–Landau (GL) description can be written explicitly in terms of the forward diffusion process and the receptive-field geometry. At tree level the coefficients are

$$r(t) = \frac{1}{\sigma^2(t)} - \frac{\alpha^2(t)}{\sigma^4(t)} |\Omega|, \quad (23)$$

$$\kappa(t) = \frac{\alpha^2(t)}{\sigma^4(t)} c_\Omega, \quad (24)$$

$$u(t) = \frac{\alpha^4(t)}{3\sigma^8(t)} |\Omega|^3. \quad (25)$$

Thus the GL parameters are completely determined by the forward diffusion statistics $(\alpha(t), \sigma(t))$ and the receptive-field geometry Ω . At the mean-field level, instability occurs when the quadratic coefficient changes sign,

$$r(t_c) = 0. \quad (26)$$

Using the expression above gives

$$\sigma^2(t_c) = \alpha^2(t_c) |\Omega|. \quad (27)$$

Since the variance-preserving process satisfies $\sigma^2(t) = 1 - \alpha^2(t)$, this yields

$$\alpha^2(t_c) = \frac{1}{1 + |\Omega|}. \quad (28)$$

For a general VP noise schedule,

$$\int_0^{t_c} \beta(s) ds = \log(1 + |\Omega|), \quad (29)$$

and for the constant schedule $\beta(t) = 1$,

$$t_c = \log(1 + |\Omega|). \quad (30)$$

This provides an explicit tree-level estimate for the time at which the long-wavelength instability underlying the critical regime appears.

B Analysis of soft modes in generic equivariant and local architectures

Since the behavior near to the equilibrium point is controlled by the linearization, we can characterize the instabilities of arbitrarily complex neural architectures by studying its Jacobian. We consider a scalar field $x = (x_i)_{i \in \Lambda}$, $x_i \in \mathbb{R}$, defined on a d -dimensional periodic lattice $\Lambda = (\mathbb{Z}/L\mathbb{Z})^d$. A trained neural architecture at fixed diffusion time t induces a vector field $s_t : \mathbb{R}^\Lambda \rightarrow \mathbb{R}^\Lambda$, $x \mapsto s_t(x)$, which we assume satisfies the following structural properties:

1. **Differentiability:** s_t is C^3 in a neighborhood of a symmetric branch.
2. **Locality:** there exists a finite radius R such that $s_{t,i}(x)$ depends only on $\{x_{i+u} : u \in \Omega_R\}$.
3. **Translation equivariance:** $s_t(\tau_a x) = \tau_a s_t(x)$ for all lattice shifts a .
4. **Local \mathbb{Z}_2 symmetry:** $s_t(-x) = -s_t(x)$.

We expand the dynamics around a translation-invariant symmetric branch, which without loss of generality we take to be $x = 0$. The linearization is given by a Jacobian operator

$$(H(t)y)_i = \sum_{u \in \Omega_R} K_t(u) y_{i+u},$$

which is a finite-range convolution operator. As a consequence of translation equivariance, the Fourier modes diagonalize the linearized dynamics: $\widehat{H}y(k) = \lambda(k, t) \widehat{y}(k)$, $\lambda(k, t) = \sum_{u \in \Omega_R} K_t(u) e^{ik \cdot u}$. The function $\lambda(k, t)$ is real and even in k , and plays the role of a dispersion relation for linear perturbations. A linear instability occurs when the spectral maximum of $\lambda(k, t)$ reaches zero:

$$\max_k \lambda(k, t_c) = 0.$$

The set of maximizing wavevectors $\mathcal{M} = \arg \max_k \lambda(k, t_c)$ defines the *soft modes* of the system. These modes become marginal at t_c and dominate the dynamics near the transition. The geometry of \mathcal{M} determines the structure of the emerging patterns. Near a maximizer k_* , the dispersion admits a smooth expansion

$$\lambda(k, t) = -r(t) - \frac{1}{2}(k - k_*)^\top A(t)(k - k_*) + O(|k - k_*|^4),$$

where $r(t_c) = 0$ and $A(t)$ is positive semidefinite. The coefficient $r(t)$ plays the role of an effective mass.

B.1 Effective long-wavelength description

Close to a point of instability, the dynamics reduces to the subspace spanned by the soft modes. Writing the field as a superposition of slowly varying amplitudes modulating the critical wavevectors, one obtains a local effective theory whose form is fixed by symmetry and locality. The structure of this theory depends on the set of maximizing eigenvectors \mathcal{M} :

- **Single maximum at $k_* = 0$:** The soft field is a real scalar $\phi(x)$ varying on long spatial scales. The effective theory takes the form

$$\mathcal{F}[\phi] = \int d^d r \left[\frac{1}{2} r(t) \phi^2 + \frac{1}{2} \kappa_{\mu\nu} \partial_\mu \phi \partial_\nu \phi + \frac{u(t)}{4} \phi^4 + \dots \right],$$

corresponding to the standard scalar ϕ^4 (Ising) theory.

- **Single commensurate maximum at $k_* \neq 0$:** The field decomposes as

$$x_i \approx \phi(x) e^{ik_* \cdot i},$$

with a real amplitude ϕ . The effective theory remains scalar ϕ^4 , but describes a *modulated* order parameter.

- **Multiple symmetry-related maxima:** The soft sector becomes multi-component,

$$x_i \approx \sum_a \phi_a(x) e^{ik_a \cdot i},$$

and the effective theory is a coupled Landau functional for the amplitudes $\{\phi_a\}$, reflecting competing ordering channels.

Therefore, the specific nature of the soft mode instability can be complex in real architectures with several possible kinds of behavior. However, importantly this can be fully understood by studying its linearization and several important properties follow directly from generic constraints like translational invariance. Note that multiple points of instability usually exist, possibly associated with different sets of soft modes.

C Supplementary Methods: Patch Model Experiments

This section describes in detail the numerical experiments used to study the emergence of spatial structure in the reverse dynamics of the patch diffusion model. All procedures described here correspond directly to the code used to generate the figures in the main text.

C.1 Patch dictionary

The generative model is defined using a discrete dictionary of binary 5×5 patches. Each patch takes values in $\{-1, 1\}^{5 \times 5}$.

The dictionary contains:

- Eight random patterns $p_k \in \{-1, 1\}^{5 \times 5}$.
- Their sign-flipped counterparts $-p_k$ to enforce a global \mathbb{Z}_2 symmetry.
- Two uniform patterns consisting of all +1 and all -1 entries.

The resulting dictionary therefore contains ten patterns.

The prior probability distribution over patches is defined as

$$\pi_k = \begin{cases} \frac{0.1}{8}, & k = 1, \dots, 8 \\ \frac{0.9}{2}, & k = 9, 10. \end{cases} \quad (31)$$

Thus the random patches collectively carry probability 0.1 while the two uniform patterns together carry probability 0.9.

This bias toward uniform patches ensures that the global patterns represent the dominant modes of the model.

C.2 Spatial domain

The model is defined on a two-dimensional periodic lattice

$$x \in \mathbb{R}^{L \times L}$$

with

$$L = 80.$$

Periodic boundary conditions are used when extracting patch neighborhoods and computing spatial correlations.

C.3 Forward diffusion process

The forward diffusion process follows the variance-preserving stochastic differential equation

$$dx_t = -\frac{1}{2}x_t dt + dW_t. \quad (32)$$

The corresponding marginal distribution satisfies

$$x_t = \alpha(t)x_0 + \sigma(t)\varepsilon, \quad (33)$$

where

$$\alpha(t) = e^{-t/2} \quad (34)$$

$$\sigma(t) = \sqrt{1 - e^{-t}}. \quad (35)$$

C.4 Exact patch score

The score function is computed analytically from the patch dictionary. For each spatial location (i, j) we consider the 5×5 neighborhood centered at that location.

Let

$$y_{ij}$$

denote the patch extracted from the current state x_t .

The posterior probability of patch p_k is

$$w_k(i, j) \propto \pi_k \exp\left(\frac{\alpha(t)}{\sigma(t)^2} \langle p_k, y_{ij} \rangle\right). \quad (36)$$

After normalization,

$$\sum_k w_k(i, j) = 1. \quad (37)$$

The posterior mean of the central pixel of the patch is

$$m_{ij} = \sum_k w_k(i, j) p_k(0, 0). \quad (38)$$

The analytic score is then

$$s(x_t, t) = \frac{\alpha(t)m - x_t}{\sigma(t)^2}. \quad (39)$$

C.5 Reverse diffusion dynamics

The reverse SDE is

$$dx_t = \left(-\frac{1}{2}x_t - s(x_t, t) \right) dt + d\bar{W}_t. \quad (40)$$

Integration proceeds backward in time from

$$T = 50$$

to

$$t_{\min} = 10^{-3}.$$

A logarithmic time grid with 2000 steps is used:

$$t_k = \exp \left(\log T + \frac{k}{N} (\log t_{\min} - \log T) \right). \quad (41)$$

The SDE is discretized using the Euler–Maruyama scheme

$$x_{k+1} = x_k + b(x_k, t_k) \Delta t + \sqrt{|\Delta t|} \eta_k, \quad (42)$$

where

$$b(x, t) = -\frac{1}{2}x - s_\theta(x, t).$$

C.6 Pattern correlation length

Spatial structure is quantified using the correlation length of the binarized field

$$\tilde{x} = \text{sign}(x). \quad (43)$$

This corresponds to a first-moment estimator of the correlation length.

The spatial autocorrelation function is computed via FFT:

$$C(r) = \frac{1}{N} \sum_{|i-j|=r} \tilde{x}_i \tilde{x}_j. \quad (44)$$

A radial average is then computed to obtain $C(r)$ as a function of distance.

The correlation length is estimated as the first moment of the positive portion of the correlation function:

$$\xi_x = \frac{\sum_r r C(r)}{\sum_r C(r)}. \quad (45)$$

C.7 Temporal derivative

To stabilize the estimate of

$$\frac{d\xi_x}{d\log t}$$

the correlation length trajectory is smoothed using a Gaussian kernel before differentiation.

C.8 Linearized dynamics

To analyze the stability of spatial modes we estimate directional derivatives of the reverse drift

$$J(x, t) = \frac{\partial b(x, t)}{\partial x}.$$

For a direction v the directional derivative is approximated using symmetric finite differences

$$\lambda_v = \frac{v^\top [b(x + \varepsilon v, t) - b(x - \varepsilon v, t)]}{2\varepsilon}. \quad (46)$$

The finite difference step is chosen adaptively as

$$\varepsilon = \max(5 \times 10^{-5}, 10^{-3}\sigma(t)^2).$$

C.9 Fourier modes

Directional derivatives are computed along Fourier modes

$$v_{n,x}(i, j) = \cos(nk_{\min}i) \quad (47)$$

$$v_{n,y}(i, j) = \cos(nk_{\min}j) \quad (48)$$

with

$$k_{\min} = \frac{2\pi}{L}.$$

Modes up to shell $n = 6$ are evaluated.

C.10 Equilibrium correlation length

To estimate the equilibrium correlation length of fluctuations around the denoising branch we analyze the low-frequency dispersion of the Jacobian.

Let

$$\lambda_n(t)$$

denote the directional derivative for shell n .

To remove the rapidly increasing stiffness of the dynamics at small t , the spectrum is normalized by the constant mode:

$$\tilde{\lambda}_n(t) = \frac{\lambda_n(t)}{\lambda_0(t)}. \quad (49)$$

For small wavenumbers the dispersion is expected to follow

$$\tilde{\lambda}_n(t) \approx 1 + \xi_{\text{eq}}(t)^2 (nk_{\text{min}})^2. \quad (50)$$

The equilibrium correlation length is therefore estimated by fitting

$$\tilde{\lambda}_n(t) - 1 = \xi_{\text{eq}}(t)^2 (nk_{\text{min}})^2 \quad (51)$$

over the lowest Fourier shells $n = 1, 2, 3$.

C.11 Trajectory statistics

All quantities are computed for multiple independent reverse diffusion trajectories.

For visualization:

- Individual trajectories are plotted with transparency.
- Median curves are plotted in black.
- Equilibrium correlation lengths are rescaled to match the vertical range of $\xi_x(t)$ for visualization purposes.

C.12 Critical time

The theoretical critical time of the model is

$$t_c \approx \log(26). \quad (52)$$

This time corresponds to the point where the lowest spatial modes of the linearized dynamics become maximally soft. In all figures this point is indicated by a vertical dashed line.

C.13 Summary of parameters

Grid size	80×80
Patch size	5×5
Random patches	8
Uniform patches	2
Reverse time range	$T = 50$ to 10^{-3}
Integration steps	2000
Trajectories	4
Fourier shells	$n \leq 6$

All experiments reported in the paper can be reproduced using these parameters.

D Supplementary Experiments: Trained Convolutional Diffusion Models

This section describes in detail the experimental setup used to analyze pattern formation in trained diffusion models. The goal of these experiments is to reproduce, in a trained neural network, the dynamical phenomena observed in the analytic patch model. In particular, we measure the evolution of spatial correlations, the softening of Fourier modes of the reverse drift, and the effective equilibrium correlation length along the reverse diffusion trajectory.

D.1 Dataset and preprocessing

The experiments use the Fashion-MNIST dataset, which consists of grayscale images of clothing items with spatial resolution

$$28 \times 28.$$

To simplify the statistical structure of the data and emphasize spatial pattern formation, we use a binarized version of the dataset. Each pixel is converted to a binary variable using a deterministic threshold:

$$x_{ij} = \begin{cases} +1 & \text{if } p_{ij} > 0.5, \\ -1 & \text{otherwise,} \end{cases}$$

where p_{ij} denotes the normalized grayscale pixel value.

After binarization the images satisfy

$$x \in \{-1, 1\}^{28 \times 28}.$$

This preprocessing step removes grayscale variability that is unrelated to spatial organization and makes the dataset closer to a lattice spin system, which simplifies the interpretation of the correlation analysis.

D.2 Diffusion process

We train the model using the variance-preserving (VP) diffusion formulation introduced in Section 3 of the main text. The forward diffusion process satisfies the stochastic differential equation

$$dx_t = -\frac{1}{2}x_t dt + dW_t,$$

corresponding to the constant noise schedule

$$\beta(t) = 1.$$

The solution of this process can be written in closed form as

$$x_t = \alpha(t)x_0 + \sigma(t)\varepsilon, \quad \varepsilon \sim \mathcal{N}(0, I),$$

with

$$\alpha(t) = e^{-t/2}, \quad \sigma^2(t) = 1 - e^{-t}.$$

These functions determine the statistics of the noisy data distribution used during score-matching training.

The reverse-time diffusion process is given by

$$dx_t = \left(-\frac{1}{2}x_t - s_\theta(x_t, t) \right) dt + d\bar{W}_t,$$

where $s_\theta(x, t)$ denotes the learned score function.

D.3 Network architecture

The score network is implemented as a lightweight convolutional U-Net designed for small images. The network predicts the noise field $\varepsilon_\theta(x_t, t)$ used in the standard noise-prediction formulation of diffusion models.

D.3.1 Time embedding

The diffusion time t is encoded using sinusoidal embeddings

$$\phi_k(t) = \begin{cases} \sin(\omega_k t), \\ \cos(\omega_k t), \end{cases}$$

with logarithmically spaced frequencies

$$\omega_k = \exp\left(-\frac{k}{d} \log 10000\right).$$

The embedding dimension is $d = 128$. The embedding vector is processed by a two-layer multilayer perceptron with SiLU activation.

D.3.2 Convolutional backbone

The main architecture follows an encoder–decoder structure with residual blocks.

Input layer The input image

$$x_t \in \mathbb{R}^{1 \times 28 \times 28}$$

is first processed by a 3×3 convolution producing 64 channels.

Encoder The encoder consists of two resolution stages:

- Stage 1:
 - Residual block (64 channels)
 - Strided convolution downsampling (factor 2)
- Stage 2:
 - Residual block (64 \rightarrow 128 channels)
 - Strided convolution downsampling

Residual block Each residual block consists of

- Group normalization
- SiLU activation
- 3×3 convolution
- addition of projected time embedding
- Group normalization
- SiLU activation
- 3×3 convolution

If the input and output channel dimensions differ, a 1×1 convolution is used in the residual connection.

Bottleneck The bottleneck consists of two residual blocks operating at 128 channels.

Decoder The decoder mirrors the encoder structure:

- Upsampling layer
- Concatenation with skip connection
- Residual block

Two such stages are used to restore the original spatial resolution.

Output layer The final layer consists of

- Group normalization
- SiLU activation
- 3×3 convolution producing a single output channel

The network predicts the noise field $\varepsilon_\theta(x_t, t)$. The score is recovered as

$$s_\theta(x_t, t) = -\frac{\varepsilon_\theta(x_t, t)}{\sigma(t)}.$$

D.4 Training procedure

The network is trained using denoising score matching with the standard noise prediction loss

$$L(\theta) = \mathbb{E} [\|\varepsilon - \varepsilon_\theta(x_t, t)\|^2].$$

Training parameters:

Dataset	Fashion-MNIST (binarized)
Epochs	30
Batch size	256
Optimizer	AdamW
Learning rate	2×10^{-4}
Gradient clipping	1.0
Time sampling	log-uniform

Log-uniform sampling over diffusion time ensures sufficient coverage of the small-noise regime, where the reverse dynamics becomes stiff.

D.5 Reverse diffusion sampling

Samples are generated by numerically integrating the reverse SDE on a logarithmic time grid

$$t_k = \exp\left(\log T + \frac{k}{N}(\log t_{\min} - \log T)\right),$$

with parameters

$$T = 50, \quad t_{\min} = 10^{-3}, \quad N = 2000.$$

The Euler–Maruyama scheme is used for integration.

D.6 Spatial correlation analysis

To analyze spatial pattern formation we measure the correlation length of the binarized configuration

$$\tilde{x} = \text{sign}(x).$$

This again corresponds to a first-moment estimator of the correlation length.

The spatial correlation function is computed as

$$C(r; t) = \langle \tilde{x}_i \tilde{x}_j \rangle_{|i-j|=r}.$$

The correlation length is estimated using the first moment

$$\xi_x(t) = \frac{\sum_r r C(r)}{\sum_r C(r)}.$$

To stabilize the derivative, the correlation-length trajectory is smoothed with a Gaussian kernel before computing

$$\frac{d\xi_x}{d \log t}.$$

D.7 Linearized drift analysis

To probe the stability of spatial modes we measure directional derivatives of the reverse drift

$$b(x, t) = -\frac{1}{2}x - s_\theta(x, t).$$

For a perturbation direction v we estimate

$$\lambda_v = \frac{v^\top (b(x + \epsilon v, t) - b(x - \epsilon v, t))}{2\epsilon}.$$

This quantity approximates the eigenvalues of the Jacobian of the reverse drift.

D.8 Fourier modes

Directional derivatives are computed along spatial Fourier modes

$$v_{n,x}(i, j) = \cos(nk_{\min}i), \quad v_{n,y}(i, j) = \cos(nk_{\min}j),$$

where

$$k_{\min} = \frac{2\pi}{L}.$$

D.9 Equilibrium correlation length

Following the analysis of the patch model we estimate an equilibrium correlation length from the normalized dispersion relation

$$\frac{\lambda_n(t)}{\lambda_0(t)} \approx 1 + \xi_{\text{eq}}(t)^2 (nk_{\min})^2.$$

Fitting this relation over the lowest Fourier shells provides an estimate of $\xi_{\text{eq}}(t)$.

D.10 Trajectory statistics

All observables are computed across several independent reverse trajectories.

Plots show

- individual trajectories (transparent curves),
- the median trajectory (solid curve).

This representation highlights the robustness of the observed dynamical features.

D.11 Interpretation

The convolutional architecture imposes locality on the learned score field. As discussed in the theoretical analysis, this architectural constraint suppresses the global mean-field instability of the empirical score and replaces it with a spatial instability governed by a local operator.

As a result, the reverse diffusion dynamics exhibit:

- softening of long-wavelength modes,
- growth of spatial correlations,
- rapid emergence of coherent structure during generation.

These observations are consistent with the interpretation of diffusion generation as a nonequilibrium dynamical phase transition.

E Supplementary Experiments: Analysis of a Trained EDM2 Diffusion Model

To test whether the theoretical predictions developed in this work extend to realistic large-scale diffusion models, we analyze the reverse diffusion dynamics of a pretrained pixel-space diffusion model trained on ImageNet. The critical line is estimated empirically as the peak of the inferred correlation length. In contrast to the analytic patch model and the small convolutional experiments described in the main text, this model operates on natural images and is trained on a large dataset using a modern diffusion architecture.

Our goal is to determine whether the same phenomenology observed in the analytic model and in small trained networks also appears in a state-of-the-art generative model. In particular, we investigate whether the reverse diffusion trajectory exhibits the signatures predicted by the statistical–physics theory:

- softening of low-frequency spatial modes,
- growth of spatial correlation length during denoising,
- emergence of a critical window where correlations are maximal.

E.1 Model

We use a pretrained pixel-space diffusion model from the EDM2 framework. The model is trained on the ImageNet dataset at a spatial resolution of 64×64 pixels. The architecture is a large convolutional U-Net with attention layers and class conditioning.

The model predicts the denoised image $D_\theta(x, \sigma, y)$, where x is the current noisy image, σ is the noise level, and y is the class label. The reverse-time dynamics of the sampler can be written as

$$\frac{dx}{d\sigma} = b_\sigma(x, \sigma)$$

with drift field

$$b_\sigma(x, \sigma) = \frac{x - D_\theta(x, \sigma, y)}{\sigma}.$$

The variable σ therefore plays the role of the control parameter along the generation trajectory, replacing the diffusion time t used in the variance-preserving formulation discussed in the main text.

E.2 Reverse diffusion trajectories

Reverse diffusion trajectories are generated using the deterministic EDM sampler with Heun correction. The sampler integrates the reverse dynamics from a large initial noise level

$$\sigma_{\max} = 80$$

down to

$$\sigma_{\min} = 0.002.$$

The noise schedule is parameterized by

$$\sigma_i = \left(\sigma_{\max}^{1/\rho} + \frac{i}{N-1} (\sigma_{\min}^{1/\rho} - \sigma_{\max}^{1/\rho}) \right)^\rho$$

with $\rho = 7$. This schedule concentrates integration steps near the low-noise regime where the dynamics becomes stiff.

For each trajectory we record the intermediate images $x(\sigma_i)$ along the reverse diffusion path.

E.3 Continuous spatial correlation length

In the analytic patch model and the binarized MNIST experiments, spatial correlations were measured using a sign-binarized field. For natural images this estimator is too coarse, as it discards most amplitude information and artificially introduces sharp domain boundaries.

Instead we compute the correlation length from a continuous scalar image field.

First, RGB images are converted to luminance

$$\ell(x) = 0.2989R + 0.5870G + 0.1140B.$$

The spatial mean is subtracted to obtain a centered field

$$\tilde{\ell}(x) = \ell(x) - \langle \ell(x) \rangle.$$

The connected spatial correlation function is then computed as

$$C(r; \sigma) = \langle \tilde{\ell}(x) \tilde{\ell}(x+r) \rangle.$$

The spatial correlation length is estimated using the second-moment estimator

$$\xi_x(\sigma) = \sqrt{\frac{\sum_r r^2 C(r; \sigma)}{\sum_r C(r; \sigma)}}.$$

This second-moment estimator is used for continuous-valued image fields. It captures the characteristic spatial scale of image structure and evolves smoothly as large-scale organization emerges during denoising.

E.4 Linearized drift operator

To probe the stability of spatial modes we analyze the Jacobian of the reverse drift field

$$b_\sigma(x, \sigma) = \frac{x - D_\theta(x, \sigma, y)}{\sigma}.$$

Directional derivatives of the Jacobian are computed using finite differences. For a perturbation direction v we estimate

$$\lambda_v(\sigma) = \frac{v^\top [b_\sigma(x + \epsilon v, \sigma) - b_\sigma(x - \epsilon v, \sigma)]}{2\epsilon}.$$

This quantity approximates the curvature of the drift operator along the direction v .

E.5 Fourier-mode analysis

To analyze spatial instabilities we evaluate directional derivatives along Fourier modes

$$v_{n,x}(i, j) = \cos(nk_{\min} i), \quad v_{n,y}(i, j) = \cos(nk_{\min} j)$$

with

$$k_{\min} = \frac{2\pi}{L}$$

where L is the image size.

These directions probe the stability of spatial modes with increasing wavelength. The resulting quantities $\lambda_n(\sigma)$ approximate the dispersion relation of the linearized operator.

E.6 Equilibrium correlation length estimator

Following the analysis developed for the analytic model, we estimate an equilibrium correlation length from the normalized dispersion relation

$$\frac{\lambda_n(\sigma)}{\lambda_0(\sigma)} \approx 1 + \xi_{\text{eq}}(\sigma)^2 (nk_{\text{min}})^2.$$

This normalization removes the overall stiffness of the dynamics and isolates the curvature of the spatial spectrum near $k = 0$.

The estimator is obtained by fitting the low-frequency modes of the dispersion relation.

E.7 Empirical critical scale

Unlike the analytic patch model, the trained neural network does not admit a closed-form expression for the coefficient $r(\sigma)$ of the effective Ginzburg–Landau theory. Consequently the critical point cannot be determined analytically.

Instead we define an empirical critical scale σ_c as the value of σ where the estimated equilibrium correlation length reaches its maximum:

$$\sigma_c = \arg \max_{\sigma} \xi_{\text{eq}}(\sigma).$$

In the theoretical description this corresponds to the point where the quadratic coefficient $r(\sigma)$ of the effective field theory approaches zero, indicating that the lowest spatial modes become maximally soft.

E.8 Trajectory statistics

All observables are computed across multiple independent reverse diffusion trajectories.

Plots display:

- individual trajectories as transparent curves,
- the median trajectory as a solid curve.

This visualization highlights the consistency of the dynamical features across samples.

E.9 Interpretation

The results show that the reverse diffusion dynamics of a large pretrained ImageNet model exhibit the same qualitative behavior predicted by the statistical–physics framework. As the noise level decreases, long-wavelength spatial modes soften and the spatial correlation length grows, indicating the emergence of coherent structure across the image.

The correlation length reaches a maximum within a narrow window of noise levels before decreasing again as the system enters a rigid low-noise regime. This behavior is consistent with the nonequilibrium critical dynamics described in the main text, where the reverse diffusion trajectory passes through a rounded critical regime during which spatial correlations are amplified before the system settles into a stable configuration.

F Supplementary Methods: Guidance pulse experiments in a pretrained EDM2 model

This section describes the guidance pulse experiments performed on a pretrained EDM2 ImageNet diffusion model. The objective of these experiments is to test whether the critical regime identified by the dynamical analysis of the reverse process also corresponds to a window of enhanced controllability. Specifically, we ask whether a short pulse of classifier-free guidance has a stronger effect when

applied near the empirically identified critical scale than when applied at a random point along the denoising trajectory.

F.1 Model and sampling framework

We use a pretrained pixel-space EDM2 diffusion model on ImageNet at resolution 64×64 . The reverse dynamics are parameterized by the EDM noise variable σ , rather than by the variance-preserving time variable t used in the analytic patch model.

The deterministic reverse flow is written as

$$\frac{dx}{d\sigma} = b_\sigma(x, \sigma), \quad b_\sigma(x, \sigma) = \frac{x - D_\theta(x, \sigma, y)}{\sigma},$$

where $D_\theta(x, \sigma, y)$ denotes the class-conditional denoiser and y is the class label.

In the autoguided EDM2 setup, we also have an unconditional guide model $D_u(x, \sigma)$. This allows us to define a classifier-free guidance-type denoiser

$$D_{\text{cfg}}(x, \sigma, y; w) = D_\theta(x, \sigma, y) + w \left(D_\theta(x, \sigma, y) - D_u(x, \sigma) \right),$$

where w is the guidance scale.

The corresponding reverse drift under guidance is therefore

$$b_\sigma^{(w)}(x, \sigma) = \frac{x - D_{\text{cfg}}(x, \sigma, y; w)}{\sigma}.$$

Sampling is performed using the standard EDM sampler with Heun correction, with noise levels evolving from

$$\sigma_{\text{max}} = 80$$

to

$$\sigma_{\text{min}} = 0.002.$$

The noise schedule is

$$\sigma_i = \left(\sigma_{\text{max}}^{1/\rho} + \frac{i}{N-1} \left(\sigma_{\text{min}}^{1/\rho} - \sigma_{\text{max}}^{1/\rho} \right) \right)^\rho$$

with

$$\rho = 7.$$

F.2 Continuous-field dynamical analysis

To identify the critical regime of the reverse diffusion dynamics, we performed the same analysis used earlier for the EDM2 trajectories.

Continuous correlation length. Because the EDM2 model generates natural RGB images, a sign-binarized estimator is inappropriate. Instead, each image is first converted to luminance

$$\ell(x) = 0.2989 R + 0.5870 G + 0.1140 B,$$

and centered by subtracting the spatial mean:

$$\tilde{\ell}(x) = \ell(x) - \langle \ell(x) \rangle.$$

The connected spatial correlation function is computed as

$$C(r; \sigma) = \langle \tilde{\ell}(x) \tilde{\ell}(x+r) \rangle.$$

The spatial correlation length is then estimated using a second-moment estimator,

$$\xi_x(\sigma) = \sqrt{\frac{\sum_r r^2 C(r; \sigma)}{\sum_r C(r; \sigma)}}.$$

Linearized drift and low-frequency modes. To probe the stability of the reverse dynamics, we computed directional derivatives of the Jacobian of the unguided reverse drift,

$$J_\sigma(x) = \frac{\partial b_\sigma(x, \sigma)}{\partial x},$$

along Fourier modes

$$v_{n,x}(i, j) = \cos(nk_{\min} i), \quad v_{n,y}(i, j) = \cos(nk_{\min} j),$$

with

$$k_{\min} = \frac{2\pi}{L}.$$

For a direction v , the directional derivative was estimated using finite differences:

$$\lambda_v(\sigma) = \frac{v^\top [b_\sigma(x + \varepsilon v, \sigma) - b_\sigma(x - \varepsilon v, \sigma)]}{2\varepsilon}.$$

To stabilize the estimate, the finite-difference step was scaled with σ .

Equilibrium correlation length proxy. Following the same logic as in the patch model, we estimated an equilibrium correlation length from the normalized low-frequency dispersion of the Jacobian. Let $\lambda_n(\sigma)$ denote the shell-averaged low-frequency directional derivative. We fit

$$\frac{\lambda_n(\sigma)}{\lambda_0(\sigma)} \approx 1 + \xi_{\text{eq}}(\sigma)^2 (nk_{\min})^2.$$

This normalization removes the rapidly increasing overall stiffness of the drift at small σ and isolates the spatial curvature of the spectrum. The resulting quantity $\xi_{\text{eq}}(\sigma)$ serves as a proxy for the equilibrium correlation length of fluctuations around the instantaneous denoising branch.

F.3 Global critical scale estimation

A naive strategy would be to estimate a separate critical scale for each class. In practice, however, this estimate is noisy because the Jacobian-based equilibrium-length proxy is sensitive to finite-sample fluctuations.

To reduce variance, we used a global procedure. We first generated unguided trajectories for all selected classes and computed $\xi_{\text{eq}}(\sigma)$ for each trajectory. These curves were then aggregated across all classes and trajectories, and a single global critical scale was defined as

$$\sigma_c = \arg \max_{\sigma} \text{median } \xi_{\text{eq}}(\sigma).$$

This construction has two advantages:

- it suppresses class-specific noise in the equilibrium-length estimate,
- it identifies a single intervention scale that can be applied uniformly across classes.

Operationally, σ_c marks the window in which the low-frequency modes of the reverse drift are globally the softest.

F.4 Pulse-guidance intervention

After estimating the global critical scale, we ran two intervention conditions.

Critical-pulse condition. A guidance pulse of strength w_{pulse} was applied only within a short interval centered at the global critical scale:

$$w(\sigma) = \begin{cases} w_{\text{pulse}}, & \sigma \in [\sigma_c - \Delta, \sigma_c + \Delta], \\ 0, & \text{otherwise.} \end{cases}$$

Random-pulse condition. A pulse of identical strength and width was applied, but with center sampled uniformly at random in σ :

$$\sigma_{\text{rand}} \sim \text{Unif}[\sigma_{\text{min}}, \sigma_{\text{max}}],$$

and

$$w(\sigma) = \begin{cases} w_{\text{pulse}}, & \sigma \in [\sigma_{\text{rand}} - \Delta, \sigma_{\text{rand}} + \Delta], \\ 0, & \text{otherwise.} \end{cases}$$

Thus the only difference between the two conditions is the location of the pulse along the reverse trajectory.

F.5 Classes, trials, and hyperparameters

We selected 10 ImageNet classes and generated 40 samples per class and per condition.

The pulse experiment therefore consisted of

$$10 \text{ classes} \times 2 \text{ conditions} \times 40 \text{ trials}$$

for a total of 800 guided generations.

The key hyperparameters were:

Number of classes	10
Trials per class per condition	40
Critical scale	global, estimated from all classes
Pulse width	2Δ in σ
Pulse strength	fixed strong guidance scale
Conditions	critical pulse / random pulse

F.6 Class-alignment metric

To quantify whether the pulse improved semantic targeting, final generated images were evaluated with a pretrained DINOv2 ImageNet classifier.

For a generated image x , the classifier produces logits $z_c(x)$ and probabilities

$$p_c(x) = \frac{e^{z_c(x)}}{\sum_{c'} e^{z_{c'}(x)}}.$$

For a target class y , we recorded:

- the target-class logit $z_y(x)$,
- the target-class probability $p_y(x)$,
- whether the top predicted class matched the target class.

These quantities were averaged across trials for each class and condition.

F.7 Statistical comparison

For each class, we compared the critical-pulse and random-pulse conditions using the mean target probability, mean target logit, and top-1 correctness fraction. We report per-class summary tables of the form

$$\begin{aligned} \Delta p_y &= \bar{p}_y^{\text{critical}} - \bar{p}_y^{\text{random}}, \\ \Delta z_y &= \bar{z}_y^{\text{critical}} - \bar{z}_y^{\text{random}}. \end{aligned}$$

Positive values indicate that the pulse delivered near the critical scale yields better class alignment than a pulse delivered at a random point.

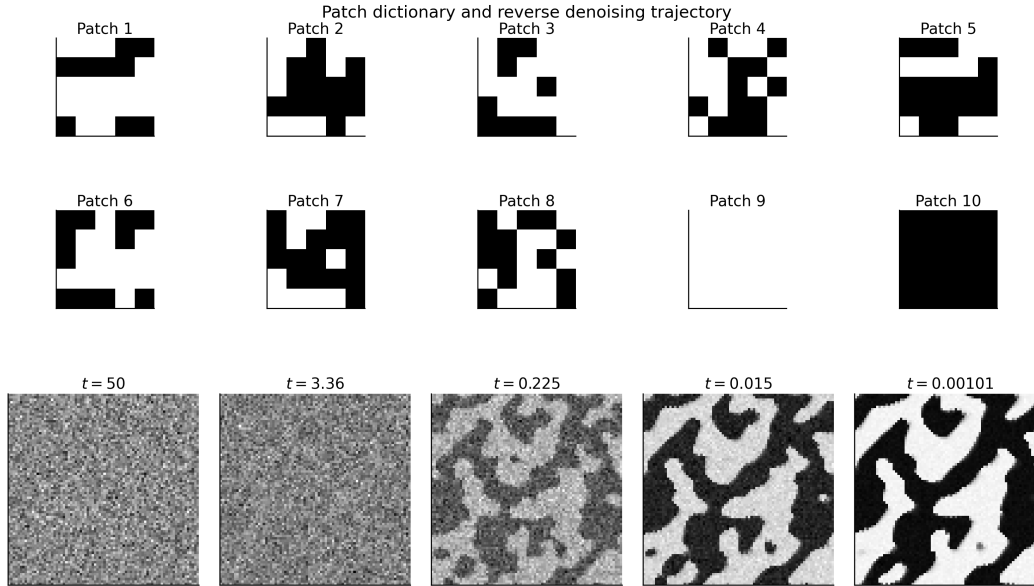


Figure 5: Patch dictionary (top) and a representative reverse denoising trajectory (bottom). Five snapshots of the evolving configuration are shown at logarithmically spaced times along the reverse diffusion path. Initially the field is dominated by noise, while at later times large coherent domains form as the dynamics selects one of the dominant global patterns.

F.8 Interpretation

The theoretical picture developed in the main text predicts that the reverse diffusion dynamics pass through a critical window in which long-wavelength modes are especially soft. In that regime, perturbations to the drift should have disproportionate influence on the macroscopic organization of the sample.

The pulse-guidance experiment tests this directly. If the critical-scale pulse outperforms the random pulse, this indicates that the identified soft-mode regime is not merely a descriptive signature of generation dynamics, but a stage at which the model is maximally susceptible to semantically structured control.

The observed improvement in class alignment under critical-time pulses supports exactly this interpretation. It shows that the critical regime is an operationally meaningful feature of the reverse diffusion process and can be exploited to intervene on generation more efficiently than by applying the same guidance signal at an arbitrary point in the denoising trajectory.

F.9 Visualization of guided and unguided trajectories

To complement the quantitative metrics, we also visualized denoising trajectories under unguided sampling and under critical-pulse sampling. For a fixed class and random seed, we plotted a sequence of intermediate denoising states across 10 logarithmically spaced values of σ .

These visualizations illustrate how the pulse intervention changes the trajectory specifically near the critical regime, while leaving the remainder of the reverse process unchanged. This makes it possible to isolate the dynamical leverage of the critical window directly at the level of the image trajectory.

G Additional results

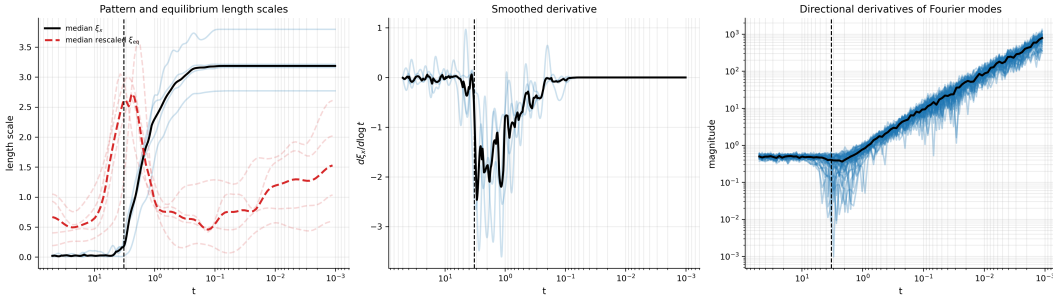


Figure 6: Quantitative analysis of pattern formation dynamics on binarized ConvNets trained on FashionMNIST.

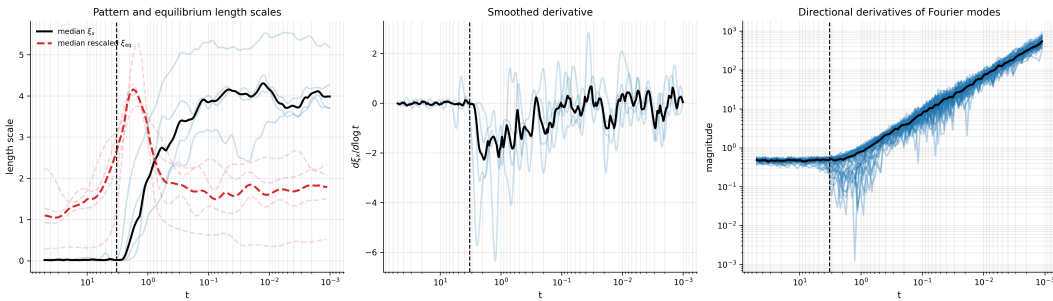


Figure 7: Quantitative analysis of pattern formation dynamics on non-binarized ConvNets trained on FashionMNIST. The critical line is estimated under the (incorrect) binary theory, so it should be interpreted as a rough estimate.

NeurIPS Paper Checklist

1. Claims

Question: Do the main claims made in the abstract and introduction accurately reflect the paper’s contributions and scope?

Answer: [Yes]

Justification: The abstract outlines the main theoretical framework and experimental results.

2. Limitations

Question: Does the paper discuss the limitations of the work performed by the authors?

Answer: [Yes]

Justification: Limitations are discussed in the ‘Conclusions and limitations’ section, especially concerning the applicability to networks that are not translationally invariant or in latent space.

3. Theory assumptions and proofs

Question: For each theoretical result, does the paper provide the full set of assumptions and a complete (and correct) proof?

Answer: [N/A]

Justification: The paper uses a physics approach based on derivations on specific models (e.g. the patch model) and general principles well-established in physics.

4. Experimental result reproducibility

Question: Does the paper fully disclose all the information needed to reproduce the main experimental results of the paper to the extent that it affects the main claims and/or conclusions of the paper (regardless of whether the code and data are provided or not)?

Answer: [Yes]

We provide all relevant experimental details and code in the supplementary.

5. Open access to data and code

Question: Does the paper provide open access to the data and code, with sufficient instructions to faithfully reproduce the main experimental results, as described in supplemental material?

Answer: [Yes]

Justification: We provide all relevant codes and all data and models we used are open source.

6. Experimental setting/details

Question: Does the paper specify all the training and test details (e.g., data splits, hyperparameters, how they were chosen, type of optimizer) necessary to understand the results?

Answer: [Yes]

Justification: Yes, we provide the training details in the supplementary.

7. Experiment statistical significance

Question: Does the paper report error bars suitably and correctly defined or other appropriate information about the statistical significance of the experiments?

Answer: [Yes]

Justification: While we do not do significant testing, we provide descriptive statistics in the figure, such as the curves for different sampled trajectories besides of the mean.

8. Experiments compute resources

Question: For each experiment, does the paper provide sufficient information on the computer resources (type of compute workers, memory, time of execution) needed to reproduce the experiments?

Answer: [N/A]

Justification: The paper uses very limited resources as it only involves the training of small models and the analysis of pre-trained models.

9. Code of ethics

Question: Does the research conducted in the paper conform, in every respect, with the NeurIPS Code of Ethics <https://neurips.cc/public/EthicsGuidelines>?

Answer: [Yes]

Justification: The paper study an abstract subject in complete accord with the code of ethics.

10. Broader impacts

Question: Does the paper discuss both potential positive societal impacts and negative societal impacts of the work performed?

Answer: [No]

Justification: This is a foundational and theoretical research, not directly connected to societal uses.

11. Safeguards

Question: Does the paper describe safeguards that have been put in place for responsible release of data or models that have a high risk for misuse (e.g., pre-trained language models, image generators, or scraped datasets)?

Answer: [N/A]

Justification: This work and its code poses no societal risk due to its theoretical nature.

12. Licenses for existing assets

Question: Are the creators or original owners of assets (e.g., code, data, models), used in the paper, properly credited and are the license and terms of use explicitly mentioned and properly respected?

Answer: [Yes]

Justification: We included references and properly cited to all open access material used here.

13. **New assets**

Question: Are new assets introduced in the paper well documented and is the documentation provided alongside the assets?

Answer: [Yes]

Justification: The coder is extensively documented.

14. **Crowdsourcing and research with human subjects**

Question: For crowdsourcing experiments and research with human subjects, does the paper include the full text of instructions given to participants and screenshots, if applicable, as well as details about compensation (if any)?

Answer: [N/A]

Justification: No human subjects.

15. **Institutional review board (IRB) approvals or equivalent for research with human subjects**

Question: Does the paper describe potential risks incurred by study participants, whether such risks were disclosed to the subjects, and whether Institutional Review Board (IRB) approvals (or an equivalent approval/review based on the requirements of your country or institution) were obtained?

Answer: [N/A]

Justification: No human subjects.

16. **Declaration of LLM usage**

Question: Does the paper describe the usage of LLMs if it is an important, original, or non-standard component of the core methods in this research? Note that if the LLM is used only for writing, editing, or formatting purposes and does *not* impact the core methodology, scientific rigor, or originality of the research, declaration is not required.

Answer: [Yes]

Justification: The usage of LLMs is reported in the acknowledgment section. LLMs were used to refine mathematical arguments, brainstorm theoretical routes and write the experimental code. All results and code were human checked afterwards. The main ideas and experimental designs come from the author alone, with LLMs taking care of several of the implementational details and minor choices.